



Image-Based Tomography of Structures to Detect Internal Abnormalities Using Inverse Approach

M. Shafiei Dizaji¹ · M. Alipour² · D.K. Harris²

Received: 25 November 2019 / Accepted: 22 April 2021 / Published online: 6 May 2021
© The Society for Experimental Mechanics, Inc 2021

Abstract

Image-based techniques have been extensively deployed in the fields of condition assessment and structural mechanics to measure surface effects such as displacements or strains under loading. 3D Digital Image Correlation (3D-DIC) is a technique frequently used to quantify full-field strain measurements. This research uses 3D-DIC to detect interior anomalies of structural components, inferred from the discrepancy in constitutive properties such as elasticity modulus distribution of a three-dimensional heterogeneous/homogeneous sample using limited full-field boundary measurements. The proposed technique is an image-based tomography approach for structural identification (St-Id) to recover unseen volumetric defect distributions within the interior of a 3D heterogeneous space of a structural component based on iterative updating of unknown or uncertain model parameters. The approach leverages full-field surface deformation measurements as ground truth coupled with a finite element model updating process that leverages a novel hybridized optimization algorithm for convergence. This paper presents a case study on a series of structural test specimens with artificial damage. A computer program was created to provide an automated iterative interface between the finite element model and an optimization package. Results of the study illustrated the successful convergence of the selected objective function and the identified elasticity modulus distributions. The resulting updated model at later stages of loading was also shown to correlate well with the ground truth experimental response. The results illustrate the potential to detect subsurface defects from surface observations and to characterize internal properties of materials from their observed mechanical surface response.

Keywords Inverse problem · 3D digital image correlation (3D-DIC) · Full-field measurement · Image based tomography · Hybrid algorithm · Optimization · Interior defects · Damage identification

Introduction

Material properties such as elastic modulus, shear modulus or Poisson's ratio are critical to both the design and evaluation processes of engineered systems ranging from buildings to

aerospace structures, as these properties serve as the link between stress and strain (constitutive law) [1–3], which describe the response of these engineered systems. In many cases, these material properties can be derived using standard testing approaches, but these tests are typically suitable to virgin materials that are not part of an existing system [4]. Typically, the measurement of these constitutive properties for existing structural systems requires a nondestructive indirect in-situ measurement that can be correlated with a specific material property, or a destructive extraction of a representative sample for traditional testing [4]. However, in many cases, these types of measurements are insufficient or representative samples cannot be extracted and alternative approaches are necessary. In these cases, an inverse engineering solution for structural identification (St-ID) aims to resolve the non-homogeneous material properties, demanding the knowledge of interior and exterior deformation fields such as displacement/strain fields and boundary conditions. One

✉ M. Shafiei Dizaji
mehrddad_shafieidizaji@uml.edu

M. Alipour
ma4cp@virginia.edu

D.K. Harris
dharris@virginia.edu

¹ Department of Mechanical Engineering, University of Massachusetts Lowell, Lowell university Ave, Lowell, MA 01854, USA

² Department of Engineering Systems and Environment, University of Virginia, 151 Engineer's Way, Charlottesville, VA 22904, USA



extension of this inverse engineering solution is in discovering the presence of internal abnormalities (e.g., internal geometric features such as voids or other types of defects), presumed as a locally heterogeneous status inferred from non-uniform stochastic elastic modulus distribution in the interior of a three-dimensional (3D) region of a sample.

Ideal solutions to this type of inverse problem require measurements of deformation fields such as displacement/strain fields internal to the body of the solid. In medical applications, internal properties of a sample can be observed by non-destructive imaging tools. An example of such tools is ultrasound devices, which depend on utilizing high-frequency sound waves to produce dynamic visual images of a sample/organs from the returning echoes traveling through the area of interest. Magnetic resonance imaging (MRI) and optical coherence tomography (OCT) are other examples of non-invasive 3D imaging technologies that rely on the detection of changes by using magnetic fields and low-coherence lights, respectively [5], which can be used to identify displacement fields from image sequences [6–11]. A more recent medical imaging technique, termed *elastography*, is based on mapping a sample's mechanical properties such as stiffness based on imaging the changes subject to known displacement fields, thus helping to detect abnormalities [8–11]. While these methods can assess the volumetric displacement of biological tissue samples, they can not be practically applied to most materials of engineering interest, such as metals, concrete, and reinforced concrete. For instance, MRI technology cannot be employed on metals and reinforced concrete because the powerful magnetic field can attract objects made from certain metals and cause them to move suddenly with great force. Nevertheless, recently, the X-ray computed tomography (XCT), a 3D imaging technique commonly used in medicine, has been broadly employed to identify the internal properties of structural components due to its high resolution, non-destructive nature and ability to clearly visualize details including internal anomalies such as different streams of defects. Moreover, XCT can be combined with the Digital Volume Correlation algorithm (DVC) to map the relative deformations between consecutive XCT images with high resolution [12]. Although this technique is very promising, it presents a series of limitations: it requires expensive and complex equipment (e.g., X-ray computed tomography scanners [13, 14]), and is applicable only to materials with a natural random internal structure (e.g., foams, bones tissue, composites [15–17]), and the correlation algorithms are computationally expensive. Moreover, the procedure to implement the XCT technology requires loading of the sample while scanning, which is difficult especially for in-situ full-scale complicated structures [18].

A proposed alternative approach to address the inverse problem in elasticity is to solely use the exterior surface measurements of a sample. From an equipment perspective,

measuring surface deformations requires only a set of cameras to capture the image of the surface of the sample during external loading. Thus, the experimental setup is significantly cheaper and less complex when compared to XCT. This approach has been successfully demonstrated to recover target material property distributions using limited surface observations with simulated and experimental data. More recently, Mei et al. [19–22] proposed a strategy to solve the inverse problem in elasticity for a simulated experiment for the shear modulus distribution using only surface deformations. Their methodology does not require a priori information about the problem domain and is based on finite element method (FEM) techniques, where the shear modulus distribution is represented as unknowns on the mesh nodes and interpolated with FEM shape functions. Mei et al. [20] tested their method on a problem domain consisting of an inclusion embedded in a homogeneous background and recovered the shear modulus distribution using simulated surface displacement fields. While their approach proved successful for the tested scenario, extension to real experimental data was not discussed and their choice of gradient-based optimization algorithm has the potential for convergence difficulties in more complex problems.

Unlike state-of-the-art methods based on internal 3D scanning (e.g., XCT), the image-based tomography approach proposed in this paper utilizes digital cameras to gather exterior full-field measurements of a sample to adjust an initial FEM model via an optimization algorithm and recover the elastic modulus distribution, from which the internal abnormalities can be inferred. Image-based techniques using digital cameras are frequently employed to measure surface displacements/strains on a sample under external loading. One of these image-based techniques, Digital Image Correlation (DIC), is a non-contact photogrammetric technique used to measure full-field deformation (2D and 3D) from a sequence of images. Deformations are measured by tracking pixel movements through correlated speckle pattern subsets from image to image, and are interpolated to describe the full-field deformation over the specimen surface. Applications of the DIC technique can be found in the literature [23–26], with examples typically used to adjust and improve the mechanical characterization of solids [27, 28]. A comprehensive treatment of DIC is available in the literature [29, 30] and not presented herein, but additional details on the DIC deployment used in this investigation are provided in a later section.

Recently, the authors took advantage of the DIC technique as a full-field measurement approach for constitutive property identification of a full-scale steel component using a St-ID approach [31–34]. The results of these previous studies demonstrated the robustness of the proposed hybrid approach for identifying uncertain/unknown system parameters (e.g., material properties and boundary conditions). In this paper, a series of laboratory experiments were developed to evaluate the

feasibility of extending this hybrid approach in an inverse problem to detect internal structural defects merely by surface measurements, without a priori postulation about the internal features of a structure.

Proposed Methodology

Building upon the premise that internal abnormalities and defects can result in external perturbations in the surface response of structural components, this work proposes to use full-field sensing of the surface as a proxy to identify hidden internal defects. To that end, the proposed technique performs modifications to the constitutive material properties (e.g., stiffness) in the affected regions while maintaining the original geometry. These modifications are driven by an optimization problem that aims to minimize the disparity between the observed surface response (e.g., strains and deformations) and its simulated numerical counterpart. The final modified stiffness distribution of the specimen after optimization will indicate potential defects in the form of regions with significantly reduced stiffness. This approach aligns with constitutive law modifications based on traditional damage-mechanics theory, in which the effective stiffness is diminished based on the history of applied loads. The ultimate goal of this work is not only to diagnose the current geometric description of a structure, but also to predict/project damage evolution of the structure, allowing for accurate evaluation of the capacity of the structural component.

The proposed approach involves an experimental test of the specimen under study, where full-field surface response is measured via DIC. A corresponding FEM model of the specimen is also built and analyzed under the same conditions as the experiment. The FEM model is dissected into a number of partitions and the stiffness of each partition is used as a design variable and iteratively modified via an optimization algorithm such that the model can mimic the experimental response. The success of the process is evaluated using an objective function that quantifies the differences between the experimental and numerical response at each iteration. At the conclusion of the optimization process, if a partition contains a defect (e.g., internal void or inclusion), its stiffness value will be adjusted through the optimization process to a value that is significantly different from the intact base material. The process will be terminated when further iterations do not result in a reduction in the objective function. The following sections outline the implementation of the proposed approach including 1) a set of laboratory experiments with the use of DIC to measure the surface load effects, 2) a numerical simulation using FEM, and 3) an optimization scheme with the definition of an objective function. Performance of the proposed approach, a sensitivity analysis of the results, and

limitations and future works will also be presented later in the paper.

Experimental Setup

In this investigation, a series of quasi-static laboratory experiments were developed including four representative A36 structural steel tensile coupon samples subjected to the same displacement-controlled loading and boundary conditions. The structural configurations used in this work are illustrated schematically in (Fig. 1(a)) and can be described as:

- 1) Configuration 1: coupon specimen without any defect, subjected to tensile load.
- 2) Configuration 2: coupon specimen with two artificially manufactured defects on the back side of the sample, subjected to tensile load.
- 3) Configuration 3: coupon specimen with one artificially manufactured defect on the back side on the top region of the sample, subjected to tensile load.
- 4) Configuration 4: coupon specimen with one artificially manufactured defect on the back side on the middle region of the sample, subjected to tensile load.

As illustrated in (Fig. 1), controlled rectangular zones of artificial damage were machined into the back side of the coupons (i.e., configurations 2–4) to simulate damage on a component that would be unseen from the measurement surface. The four testing configurations described above give rise to heterogeneous and non-uniform in-plane strain fields, (i.e., longitudinal, transverse, and shear strain components), as well as in-plane/out-of-plane displacement fields (i.e., longitudinal, transverse, and out-of-plane components).

Quasi-Static Mechanical Testing

The experimental testing program consisted of a series of quasi-static tests under uniaxial tensile loading within the elastic range of the structural steel coupon specimens. The specimens were tested using a universal servo-hydraulic testing machine. Testing was performed in displacement control (0.13 ~ 0.6 mm/min) according to the test method defined in ASTM E8 [4] on the four steel coupon specimens. The geometric dimensions of the coupon specimens are shown in (Fig. 1(b)). Also, the experimental and DIC setup are illustrated in (Fig. 2) where the Area of Interest (AOI) has been defined as the region on the specimen where the DIC measurements are compared with numerical simulations.

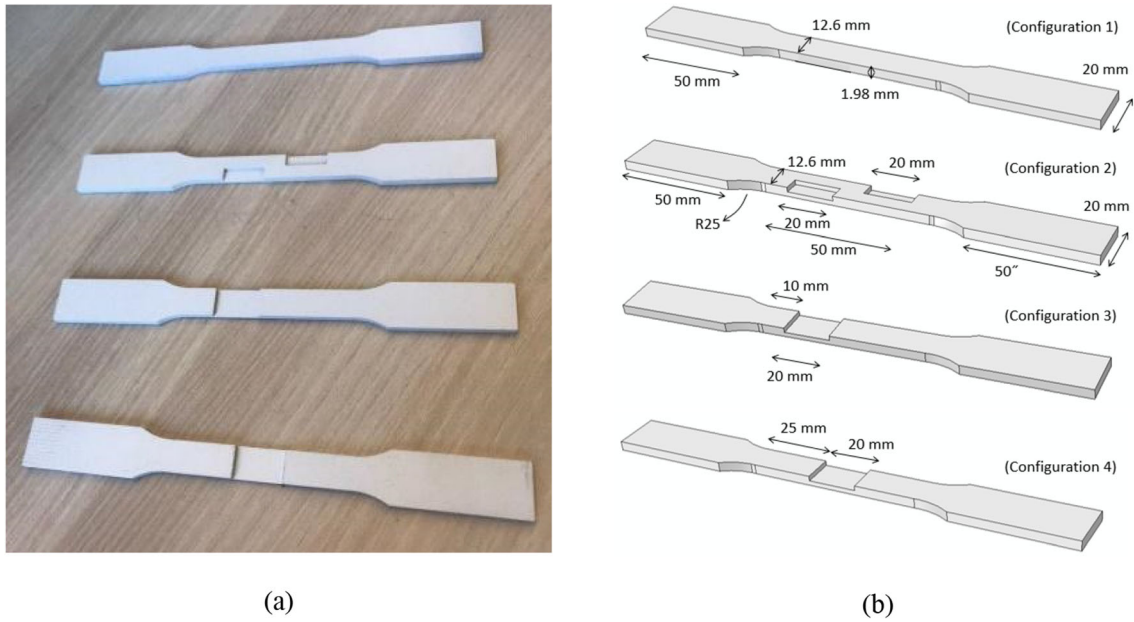


Fig. 1 Intact and simulated damage coupons (a) painted steel coupon specimens used in the experimental setups, and (b) geometric dimension of the coupon specimens

DIC Setup

The mechanical response of the specimens was measured by 3D-DIC to describe full-field surface measurements of displacement and strain of the coupons, analogous to the types of results derived from a FEM model. A commercially available DIC system from Correlated Solutions Inc. was used in this investigation [35]. The DIC system components consisted of a camera system, an image acquisition package (VicSnap), and 3D-DIC post-processing software (Vic-3D). The DIC image acquisition used one set of two stereo-paired digital cameras, 5-megapixel charge coupled device (CCD) image sensor with a resolution of 2448×2048. The camera was connected to

a C-mount optical lens (12 mm) and the acquired data was communicated to the control PC through FireWire cables. The camera pair was positioned 0.6 m from the coupon which yielded a field of view (FOV) of 0.7 × 0.7 m. For the experiment, the basic process consisted of specimen preparation, camera setup (focusing, calibration), image acquisition, and post-processing of results. Images acquired during the test were extracted every 0.5 s. Prior to testing, the surface of each specimen was covered with a fine, dense and random speckle pattern (flat white paint for base and fine tip permanent marker for pattern) for the correlation process. For the pixel tracking process in DIC, the area of interest on the speckle pattern was split into rectangular windows or “subsets” and unique

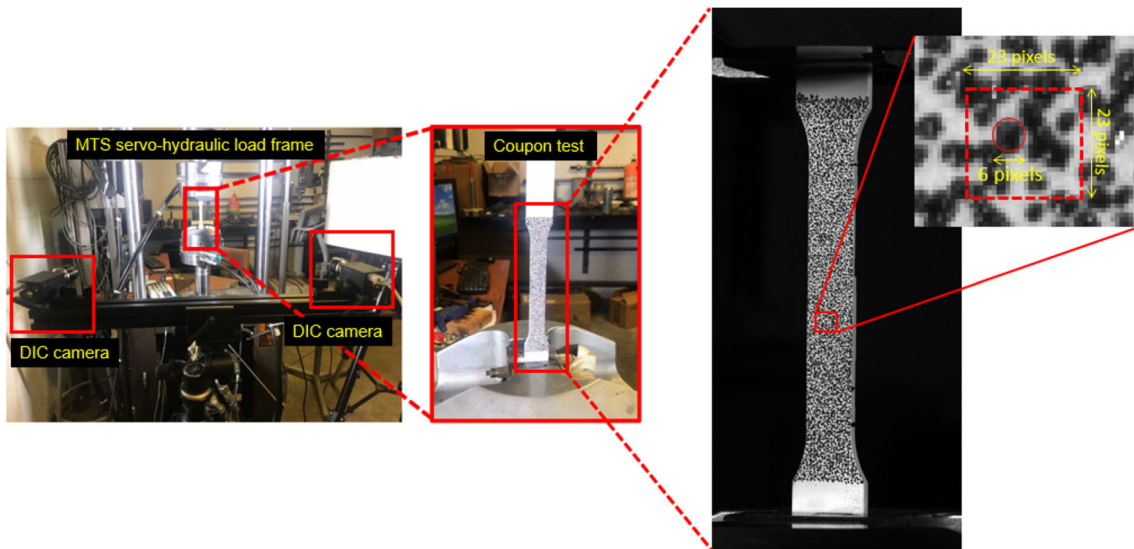


Fig. 2 Experimental and DIC setup configuration (one system including two CCD cameras)

patterns of speckles remained available within each subset to allow for tracking across subsequent frames. The patterns in the subsets were tracked on a grid of a specific “step” size, which dictated the spatial resolution of the calculated points. To achieve a fine grid of unique patterns in subsets, the selection of the subset size was determined through direct experimentation during post-processing and a square subset of 23 pixels at a step of 7 pixels was selected (Fig. 2). For more details regarding DIC setup, the reader is referred to the authors’ previous works [31–34].

Numerical Implementation

As previously noted, the finite element model updating process requires the development of an initial numerical model that can be updated based on experimentally derived behavior results. In this investigation, the FEM model of the sample was developed in ABAQUS [36, 37], a robust commercially-available FEM software package. The specimen was modeled using a total of 4300 continuum 3D hexahedral solid elements (C3D8) with full integration. The FEM model and mesh configuration of the coupon specimens are shown in (Fig. 3(a)). The region of interest in the middle of the coupon was also partitioned into a number of regions whose material properties were considered as unknown design variables in the optimization process. These partitions are depicted in (Fig. 3(b)) for configuration 2 as an example. It should be noted that ABAQUS allowed for the development of a direct interface with the optimization package, which

facilitated the iterative parameter optimization algorithm via the Python tool. In this work, the initial FEM model of the specimen was initially created using the Graphical User Interface (GUI) of ABAQUS allowing for the model developed script to be extracted. The extracted script was iteratively interfaced with the Python package, which executes the FEM computations, extracts the deformation results, and evaluates the objective function to assess the optimality/convergence of the solution at that iteration. If the stopping criteria are not met, the Python tool will then iteratively generate new parameter sets and re-run the analysis until convergence is achieved. Details of the optimization procedure are presented in the following sections.

Definition of the Objective Function

The proposed inverse-problem approach is based on solving an optimization problem to obtain the distribution of the modulus of elasticity as an unknown design variable within the FEM mesh. The basic principle of inverse problems is to minimize the discrepancy between the experimentally-measured and the numerically-computed responses by fine-tuning the unknown variables of the FEM model. In this investigation the following objective function was defined to quantify this discrepancy by including the surface strain and deformation components of the specimen, which will be pushed to minimum in the optimization process (equation (1)):

$$F(\mathbf{E}) = \sum_{k=1}^p \sum_{i=1}^m \sum_{j=1}^{n_i} \left[\left(\frac{\epsilon_{xx,ij}^{exp} - \epsilon_{xx,ij}^{num}(\mathbf{E})}{\epsilon_{xx,ij}^{exp}} \right)^2 + \left(\frac{\epsilon_{yy,ij}^{exp} - \epsilon_{yy,ij}^{num}(\mathbf{E})}{\epsilon_{yy,ij}^{exp}} \right)^2 + \left(\frac{\epsilon_{xy,ij}^{exp} - \epsilon_{xy,ij}^{num}(\mathbf{E})}{\epsilon_{xy,ij}^{exp}} \right)^2 + \left(\frac{\delta_{yy,ij}^{exp} - \delta_{yy,ij}^{num}(\mathbf{E})}{\delta_{yy,ij}^{exp}} \right)^2 \right] \tag{1}$$

Where \mathbf{E} is the vector of unknown design variables which are the constitutive properties of the model partitions, p is the number of experimental tests ($p = 1$ in this work), m is the number of load steps ($m = 20$ in this work) and n_i the number of data points in the DIC measurement at load step i . The subscripts **exp** and **num** indicate the experimental and numerical responses, respectively. The three components of the strain tensor and the longitudinal component of displacement are represented by ϵ_{xx}^{exp} , ϵ_{yy}^{exp} , ϵ_{xy}^{exp} and δ_{yy}^{exp} respectively that are extracted at a point i of coordinates x_i at time t . Similarly, ϵ_{xx}^{num} , ϵ_{yy}^{num} , ϵ_{xy}^{num} and δ_{yy}^{num} represent the corresponding values computed from the FEM model. As the numerical and experimental components of the response are developed through different procedures, for their accurate comparison within the objective function, it is necessary to interpolate the results from

DIC and FEM onto a common mesh grid. With both results mapped to this common grid, the discrepancy between FEM and DIC results can be calculated using (equation (1)) and used within the optimization process [31–34]. The components of the proposed objective function are also schematically shown in (Fig. 4).

Proper design of the objective function can help prevent numerical issues associated with non-unique solutions. While from a purely mechanical point of view, it would be expected that such an approach could yield non-unique solutions, a successful solution is possible by using a variety of load steps and boundary strains/displacement data sets from multiple load configurations, sequentially applied at discrete locations around the specimen [31–34]. Therefore, a larger value of m in the objective function increases the chance of ensuring

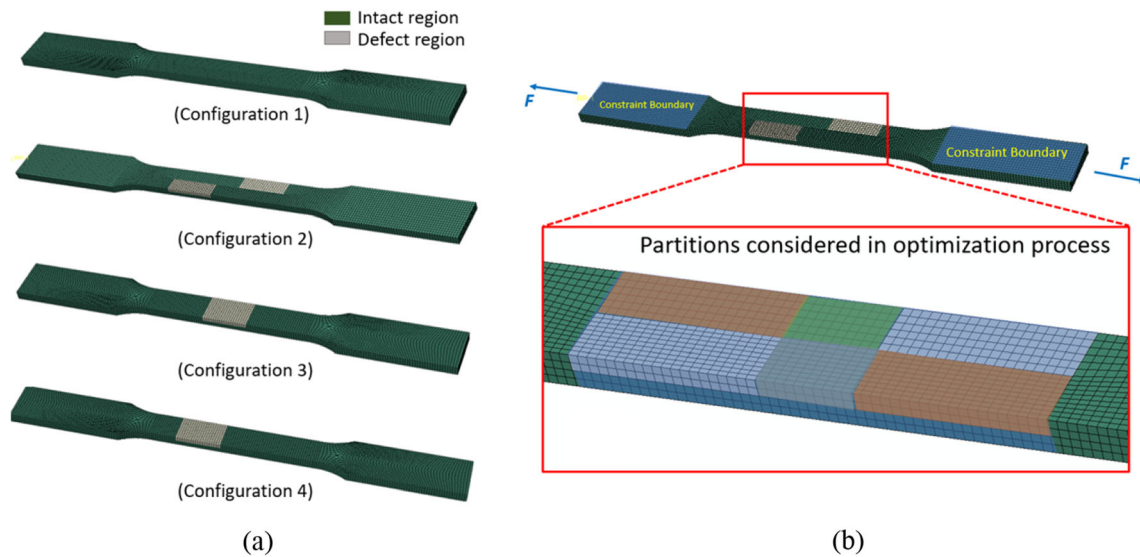


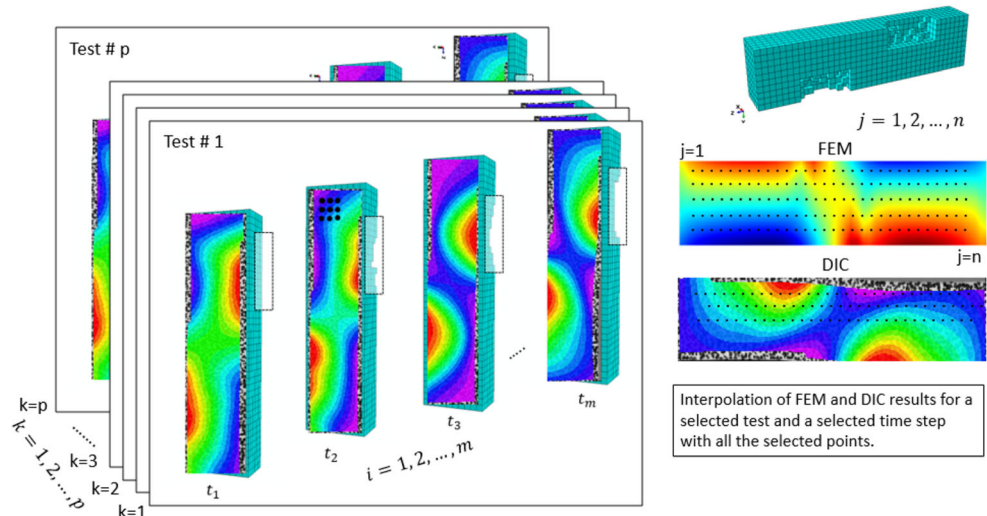
Fig. 3 (a) FEM model of the coupons, and (b) constraint boundary conditions, the direction of external loading and the partitioned regions considered in optimization process for configuration 2

uniqueness of the final solution, while also incurring a higher computational cost. Another reason for using a large value of m is to combat the effect of random noise and uncertainties in the accuracy of the full-field DIC measurements at each load step. Some of the sources of noise in the measurements include lighting fluctuations, glare, irregularities, and poor quality of speckle pattern, as well as noise resulting from image acquisition (e.g., sensor noise) and quantization [35]. Moreover, interpolation of DIC and FEM can also be a possible source of uncertainties. Therefore, to decrease such uncertainties, a large value for m was chosen in this work ($m = 20$). To offset the resulting increase in computational cost, parallel optimization was used.

Description of Optimization Techniques

In this work, a hybrid approach combining a genetic algorithm (GA) [38] and a limited-memory Broyden-Fletcher-Goldfarb-Shanno algorithm (L-BFGS-B), is introduced and used to solve the optimization problem. The genetic algorithm (GA) was used to perform a broad preliminary search in the solution space for locating the neighborhood of the solution. Subsequently, the L-BFGS-B algorithm was employed to start from the final solution provided by the GA and to further refine the solution toward an optimal state. This design of the optimization scheme was inspired by the previous literature that has shown that in problems involving a large number of parameters, a combination of these two techniques can

Fig. 4 Components of the objective function



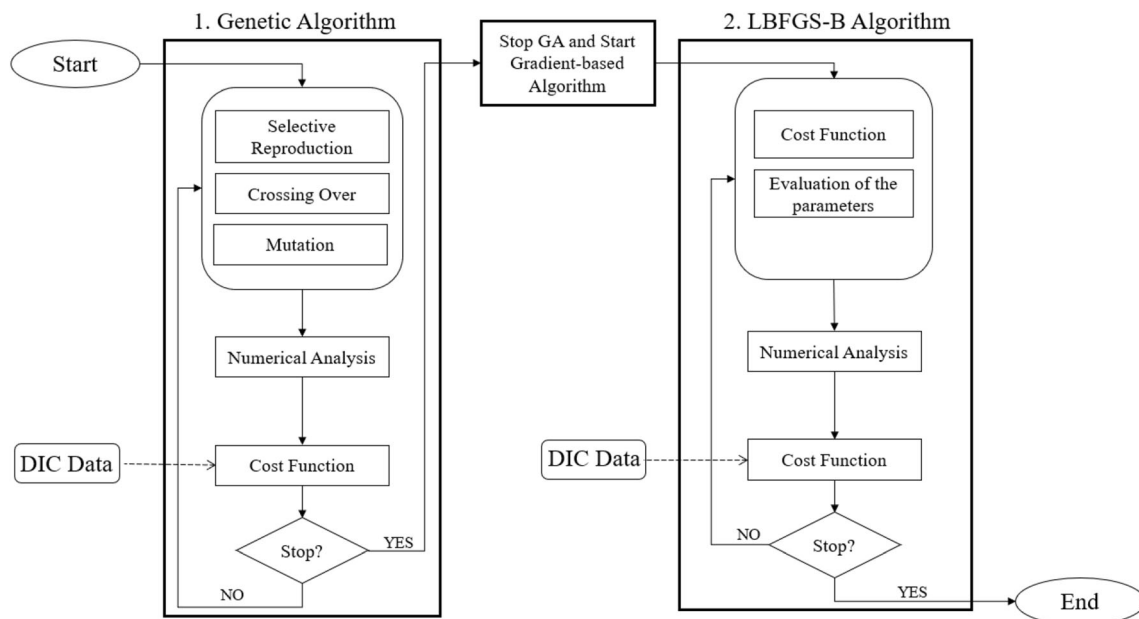


Fig. 5 Overview of the proposed optimization approach

yield superior optimization performance [39]. Figure 5 illustrates a basic flowchart of the hybrid optimization approach adopted in this work. First, a genetic optimization step is employed to explore the space of parameters and locate the approximate region of the optimum solution. After reaching a certain number of iterations, which is selected according to the size of the problem and computational cost, the GA halts (stopping criteria). After this point, the global optimum is used as a starting point for a finer local optimization to “polish” the optimum to a greater accuracy. In this second step, a gradient-based method (L-BFGS-B) is utilized to continue the search within the approximate region to quickly converge on the precise location of the optimum solution. As a result of this setup, the favorable characteristics of both methods, namely the efficient exploration of the space by the GA and the superior convergence of the gradient-based methods, are leveraged to achieve an efficient optimization. The stopping criteria for the L-BFGS-B algorithm is realized when there is no more significant decrease in the objective function.

Similar to other optimization methods, a feasible initial guess for the parameters is used to start the process. The initial guess is used to generate an initial FEM model which, upon analysis, is evaluated within the objective function. If the

stopping criteria are not met, a new solution is generated through a set of operations in the GA (e.g., selective reproduction, crossover, and mutation). The basic operations involved in the design of the GA developed in this study have been documented in various studies by Dizaji et al. [31–34]. The new solution gives rise to an updated FEM model and the process is repeated as necessary. Once the stopping criteria are satisfied, the final solution of GA is used to initiate the gradient-based scheme (L-BFGS-B) which takes the best GA solution as its starting point to further refine the GA solution. This process will continue to minimize the objective function (equation (1)) until the convergence criteria are satisfied and the final optimal solution is identified. Table 1 presents the set of optimization hyper-parameters used with GA based on the literature [40, 41], where N_{pop} , N_{elites} and N_{mut} represent the initial population, the population of elites which go directly to the next generation, and those randomly selected for mutation, respectively. Additionally, μ represents the probability rate of mutation, N_{pairs} denotes the selecting parents for mating, and $iterations$ describe the stopping criteria for termination.

In the L-BFGS-B algorithm, the objective function is approximated by a second-order Taylor series around the current design variables. As a result, this method requires the evaluation of the objective function and its gradient with respect to the design variables (modulus of elasticity) [42, 43]. The input arguments for the L-BFGS-B subroutine are the gradient of the objective function with respect to the unknown elasticity modulus distribution and the functional value at each minimization step. The subroutine then returns with an updated estimate of the parameters and this process is repeated until the change in the objective function is smaller than a specified

Table 1 Parameters of the genetic algorithm (GA) for the three identification tests for the first configuration

GA parameters	N_{pop}	N_{elites}	N_{mut}	μ	N_{pairs}	$Iterations$
Value	20	2	4	0.04	14	500

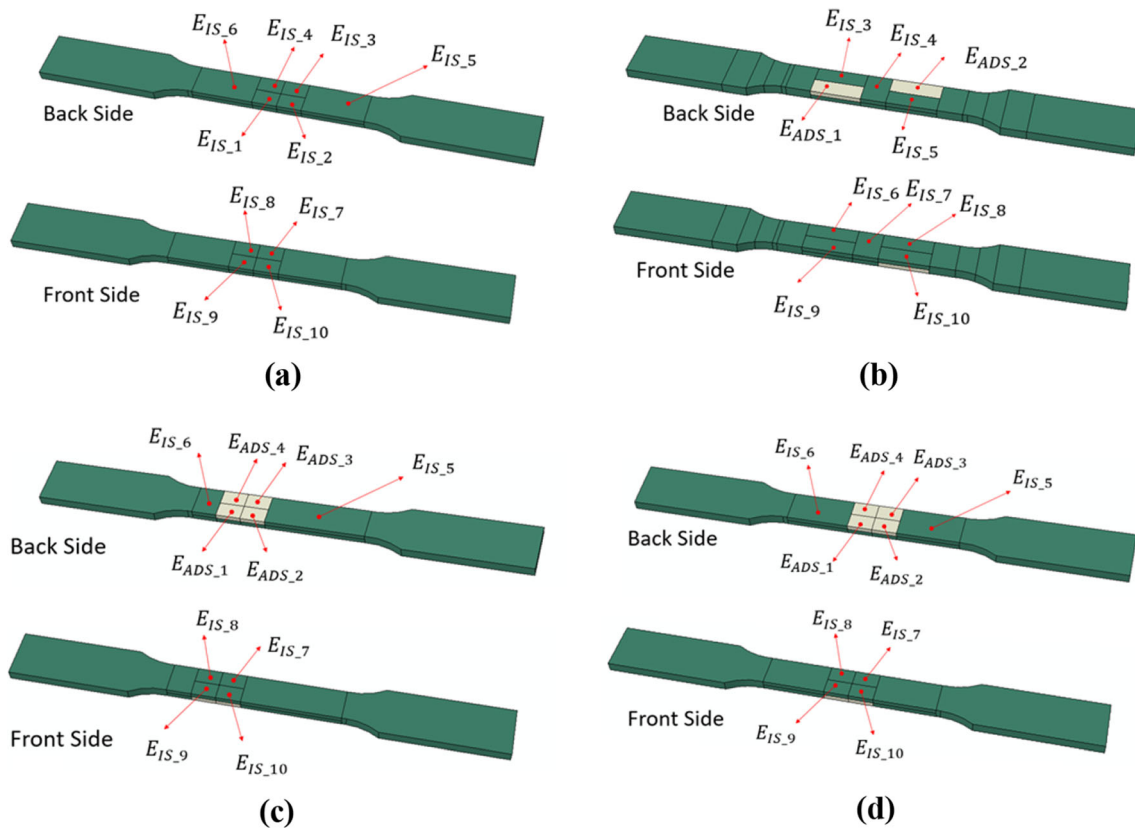


Fig. 6 Divided partitions of the configurations to import into optimization process, (a) configuration 1, (b) configuration 2, (c) configuration 3, and (d) configuration 4

tolerance. To implement the L-BFGS-B algorithm, an open-source python optimization package was used (https://docs.scipy.org/doc/scipy/reference/generated/scipy.optimize.fmin_l_bfgs_b.html).

Results and Discussion

This section presents the results of the proposed approach implemented using the four coupon specimens previously depicted in (Fig. 1). For the defined configurations, the initial FEM models of the coupons were partitioned into 10 sections as shown in (Fig. 6) and the material properties of each partition were considered as design variables within the updating process. The selection of the 10 partitions provided a rational configuration to locate the vicinity of damage for this evaluation; however, further partitioning is feasible, but at an increased computational cost due to an expanded search region within the optimization process. In this work, defects on the unseen side of the model were constrained to locations that aligned with separate partitions, which limits the search space, but ensures that the entire structural component response is considered. The partitions considered within the optimization process for all the configurations are illustrated in (Fig. 6). It should be noted that in this figure, E_{ADS} and E_{IS} are acronyms

for the elastic modulus of the artificially damaged section (ADS) and the intact section (IS), respectively. At the conclusion of the optimization process, the value of the elastic modulus for the partitions belonging to defects are expected to decrease dramatically to reflect the existence of defects in that partition, similar to the observations within the simulated experiments. Conversely, the values for the intact base material are expected to converge to target properties of the material under study.

Defect Detection Using Simulated Experiment

To evaluate the initial feasibility of the proposed approach using simulated measurements, a FEM model of the coupon specimen with simulated defects of configuration 2 (Fig. 1) was created and analyzed within the elastic range. The objective was to evaluate the feasibility using idealized surface measurements (i.e., full-field strain and displacement measurements) analogous to those derived from DIC measurements. Table 2 shows the initial values randomly selected within the feasible range (maximum and minimum values) used as the initial guess for the parameters in the optimization procedure. To demonstrate the performance of the proposed approach, (equation (2)) computes the percentage change of the design variables defined as:

Table 2 Initial, minimum, maximum, updated and target values of the updating parameters for configuration 2

E (MPa)	E_1^{ADS}	E_2^{ADS}	E_1^{IS}	E_2^{IS}	E_3^{IS}	E_4^{IS}	E_5^{IS}	E_6^{IS}	E_7^{IS}	E_8^{IS}
Initial	150,000	180,000	110,000	300,000	220,000	90,000	120,000	50,000	280,000	320,000
min	50,000	50,000	50,000	50,000	50,000	50,000	50,000	50,000	50,000	50,000
max	450,000	450,000	450,000	450,000	450,000	450,000	450,000	450,000	450,000	450,000
Updated	1122	2050	199,223	200,776	197,990	201,999	199,001	200,333	200,888	201,992
Expected Value	0.0	0.0	200,000	200,000	200,000	200,000	200,000	200,000	200,000	200,000
E_T (%)	-99.4	-98.9	-0.38	+0.38	-0.1	+0.99	-0.49	+0.16	+0.44	+0.99

$$E_T = \frac{E_{updated} - E_m}{E_m} \times 100 \quad (2)$$

where E_m was assumed as 200 GPa for the idealized modulus of elasticity of the coupon made of A36 steel [4]. It should also be noted that the target values for the damaged section (E_1^{ADS} and E_2^{ADS}) are given as zero in Table 2 signifying the absence of the base material.

As can be seen in Table 2, the partitions corresponding to the simulated defects, E_1^{ADS} and E_2^{ADS} , exhibit dramatic reductions equal to 99.4 and 98.9%, respectively, demonstrating that the defects were recovered properly. Simultaneously, all of the intact regions are shown to converge to within 1% of the target modulus of elasticity. These initial results demonstrated the feasibility of the proposed St-ID approach, prompting further evaluation using the proposed full-field experimental approach.

Defect Detection Using Experimental 3D DIC Measurements

To evaluate the performance of the proposed approach using real-world data, an experimental study was conducted using the coupon specimens with machined damage previously shown in (Fig. 1), the FEM modeling procedures described before, and the partitions shown in (Fig. 6). Using the proposed hybrid optimization approach, the minimization of the objective function was performed for 500 epochs where the first 50 epochs utilized the GA and the optimization process for the remaining epochs were performed using the L-BFGS-B method. It should be noted that the starting point of the L-BFGS-B algorithm is the last optimal point obtained from the GA. Summary of the results for the elastic modulus of the selected partitions before and after the optimization process for all configurations is presented in Table 3. As expected, it was observed that the elastic modulus belonging to the defect regions converged to significantly smaller values when compared to the regions without any defect features. These results confirmed that the proposed approach was capable of

effectively inferring the existence of defect regions from constitutive properties of the material. The convergence of the objective functions for all the configurations is presented in (Fig. 7). According to the results shown in Table 3 and (Fig. 7), it can be concluded that the proposed approach has the capability of converging to the desired global minimum.

For configuration 2, the optimization convergence of the objective function and elastic modulus of the partitioned sections are shown in (Fig. 8(a-b)). These plots show that both the objective function and the moduli of elasticity of the partitions quickly converge to stable plateaus (objective function to zero, and modulus of elasticity of intact and defective regions to 200GPa and zero, respectively). Moreover, in order to show the superiority of the proposed algorithm, the optimization process was conducted for three separate cases: 1) only GA was used for optimization, 2) only the gradient-based algorithm was used for optimization and 3) Hybridized optimization scheme was used. As seen in (Fig. 8(a)), using the proposed hybrid algorithm, the objective function has decreased more than the two base algorithms when applied alone. This demonstrates the efficiency of the hybridized optimization scheme in reducing the objective function. Moreover, the initial values and corresponding optimized solutions illustrated in (Fig. 8(c)) show proper convergence of the initial values toward their expected solutions. It should be noted that for each partitioned section, a different initial value was selected to show the capability of the proposed method in converging to the expected target value accordingly regardless of the starting point. As can be seen from (Fig. 8 (b-c)), even though initial design variables were randomly-assigned, their final updated values successfully converged to the correct expected target values.

The full-field strain measurements from DIC and FEM, along with the absolute error, before and after model updating, are shown in (Fig. 9) where the initial FEM model yields distinctly different contour patterns for the longitudinal strain than the experimental response, but following convergence to the final solution, the patterns nearly mirror each other. Through this convergence, the error, which describes the

Table 3 Summary of differences between elasticity modulus of the selected partitions before and after optimization process

Configuration 1										
E (MPa)	E_1^{IS}	E_2^{IS}	E_3^{IS}	E_4^{IS}	E_5^{IS}	E_6^{IS}	E_7^{IS}	E_8^{IS}	E_9^{IS}	E_{10}^{IS}
Initial	420,000	160,000	180,000	220,000	120,000	70,000	80,000	110,000	220,000	400,000
Updated	208,998	191,114	203,224	195,444	198,001	188,001	189,001	196,555	202,114	210,012
Expected Value	200,000	200,000	200,000	200,000	200,000	200,000	200,000	200,000	200,000	200,000
E_T (%)	+4.5	-4.4	+1.6	-2.5	-1.0	-6.0	-5.5	-2.0	+1.3	+5.0
Configuration 2										
E (MPa)	E_1^{ADS}	E_2^{ADS}	E_3^{IS}	E_4^{IS}	E_5^{IS}	E_6^{IS}	E_7^{IS}	E_8^{IS}	E_9^{IS}	E_{10}^{IS}
Initial	150,000	180,000	110,000	300,000	220,000	90,000	120,000	50,000	280,000	320,000
Updated Value	6557	9122	189,223	208,776	191,990	209,999	189,001	206,333	204,888	209,992
Expected Value	0.0	0.0	200,000	200,000	200,000	200,000	200,000	200,000	200,000	200,000
E_T (%)	-96.0	-95.0	-5.5	+4.4	-4.0	+5.0	-5.5	+3.3	+2.5	+4.5
Configuration 3										
E (MPa)	E_1^{ADS}	E_2^{ADS}	E_3^{ADS}	E_4^{ADS}	E_5^{IS}	E_6^{IS}	E_7^{IS}	E_8^{IS}	E_9^{IS}	E_{10}^{IS}
Initial	110,000	250,000	130,000	290,000	180,000	60,000	220,000	180,000	250,000	420,000
After	7445	8445	9984	8554	189,222	179,000	208,000	191,224	206,002	210,111
Ideal	0.0	0.0	200,000	200,000	200,000	200,000	200,000	200,000	200,000	200,000
E_T (%)	-96.0	-95.7	-95.0	-95.7	-5.5	-10.5	+4.0	-4.4	+3.0	+5.0
Configuration 4										
E (MPa)	E_1^{ADS}	E_2^{ADS}	E_3^{ADS}	E_4^{ADS}	E_5^{IS}	E_6^{IS}	E_7^{IS}	E_8^{IS}	E_9^{IS}	E_{10}^{IS}
Initial	170,000	220,000	280,000	130,000	100,000	140,000	220,000	170,000	70,000	150,000
Updated Value	11,224	8225	9879	5469	181,003	195,224	211,225	194,225	179,887	190,336
Expected Value	0.0	0.0	200,000	200,000	200,000	200,000	200,000	200,000	200,000	200,000
E_T (%)	-94.0	-95.9	-95.0	-97.0	-9.5	-2.4	+5.5	-3.0	-10.5	-5.0

differences between the model prediction and experimental results, drops an order of magnitude from the initial prediction.

Optimization Robustness

Non-convex optimization problems can have several different local minima resulting in different non-unique solutions to the

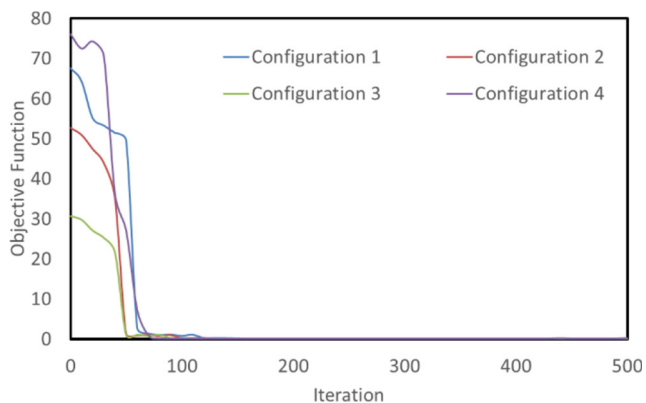


Fig. 7 Convergence of the objective function for the defined configurations

same discretized problem given different starting points and parameters of the algorithms. Global optimization methods are known to have difficulty handling problems of the size of a typical inverse problem with a large number of design variables [38–41]. In this work, two strategies were employed to overcome optimization difficulties, namely combining the global GA technique with a local gradient-based method, as well as using additional results derived from the use of multiple load steps increments (i.e., 20 load steps). To investigate the robustness of the proposed approach and ensure that the results were not sensitive to and dependent on the initial values, a series of iterations with different initial values were performed (Table 4). Four sets of randomly-generated initial starting points for the modulus of elasticity of the partitions were selected and the values of E_1^{ADS} , E_2^{ADS} and E_3^{IS} were used to evaluate the optimization performance with their convergence trends plotted in (Fig. 10). As can be noted from (Fig. 9(a - c)), even though the initial points are selected randomly for the 4 initial sets, the proposed algorithm consistently converges to the optimal values. Also, the initial values and corresponding optimized solutions for different sets of initial scenarios are illustrated in (Fig. 11). As shown in (Fig. 11), even though the initial values are selected randomly, the

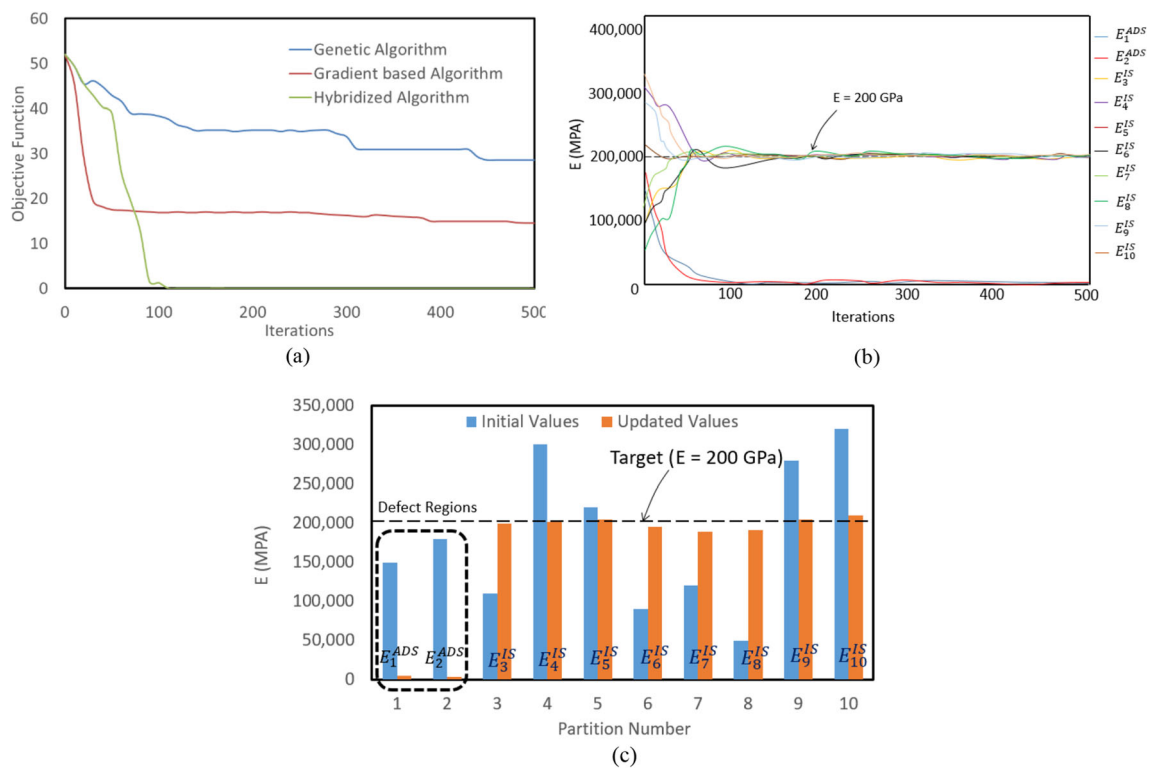


Fig. 8 (a) objective function convergence for different optimization algorithms, (b) elasticity modulus convergence, and (c) initial and final values of design variables

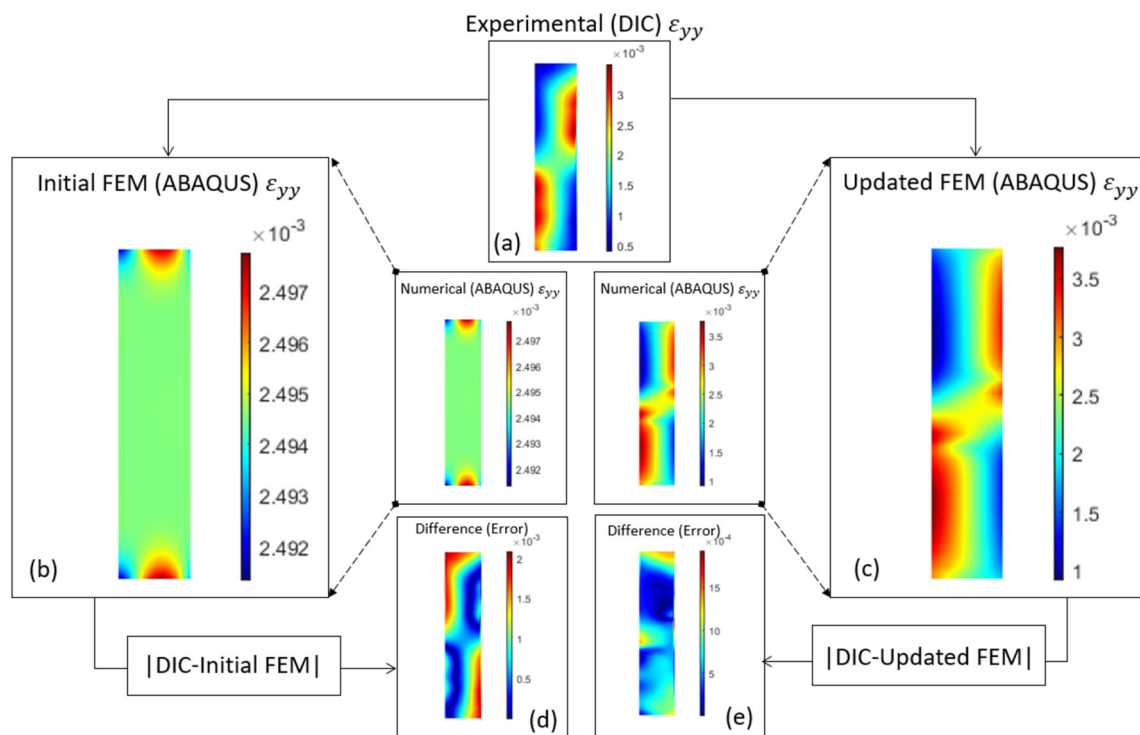


Fig. 9 Full-field measurements obtained from DIC and FE, along with the absolute error, before and after model updating (a) 3D DIC results, (b) initial FEM results, (c) updated FEM model, (d) the error between DIC and initial model, and (e) the error between DIC and updated model

Table 4 Summary of elastic modulus convergence for selected partitions for different parameter initializations (Configuration 2)

Initial set 1										
E (MPa)	E_1^{ADS}	E_2^{ADS}	E_3^{IS}	E_4^{IS}	E_5^{IS}	E_6^{IS}	E_7^{IS}	E_8^{IS}	E_9^{IS}	E_{10}^{IS}
Initial	250,000	150,000	180,000	250,000	160,000	50,000	110,000	80,000	220,000	400,000
Updated	5445	7889	188,811	220,110	192,001	180,330	202,001	190,111	200,002	209,002
Expected	0.0	0.0	200,000	200,000	200,000	200,000	200,000	200,000	200,000	200,000
E_T (%)	-97.0	-96.0	-5.6	+10.0	-4.0	-9.8	+1.0	-5.0	+0.0	+4.5
Initial set 2										
E (MPa)	E_1^{ADS}	E_2^{ADS}	E_3^{IS}	E_4^{IS}	E_5^{IS}	E_6^{IS}	E_7^{IS}	E_8^{IS}	E_9^{IS}	E_{10}^{IS}
Initial	100,000	225,000	160,000	270,000	170,000	70,000	150,000	110,000	250,000	420,000
Updated	7700	8098	203,033	210,222	200,332	199,003	201,000	203,003	210,993	220,223
Expected	0.0	0.0	200,000	200,000	200,000	200,000	200,000	200,000	200,000	200,000
E_T (%)	-96.0	-95.9	+1.5	+5.1	+0.2	-0.5	+0.5	+1.5	+5.5	+10.0
Initial set 3										
E (MPa)	E_1^{ADS}	E_2^{ADS}	E_3^{IS}	E_4^{IS}	E_5^{IS}	E_6^{IS}	E_7^{IS}	E_8^{IS}	E_9^{IS}	E_{10}^{IS}
Initial	150,000	170,000	220,000	100,000	60,000	220,000	80,000	140,000	110,000	90,000
Updated	8955	6773	200,322	188,555	192,222	200,433	179,007	201,222	205,055	200,443
Expected	0.0	0.0	200,000	200,000	200,000	200,000	200,000	200,000	200,000	200,000
E_T (%)	-95.0	-96.6	+0.2	-5.7	-3.9	+0.2	-10.5	+0.6	+2.5	+0.2
Initial set 4										
E (MPa)	E_1^{ADS}	E_2^{ADS}	E_3^{IS}	E_4^{IS}	E_5^{IS}	E_6^{IS}	E_7^{IS}	E_8^{IS}	E_9^{IS}	E_{10}^{IS}
Initial	270,000	200,000	230,000	150,000	110,000	130,000	210,000	170,000	70,000	150,000
Updated	5445	7889	204,444	199,994	188,444	199,433	200,345	192,022	195,045	197,331
Expected	0.0	0.0	200,000	200,000	200,000	200,000	200,000	200,000	200,000	200,000
E_T (%)	-97.3	-96.0	+2.2	-0.0	-5.8	-0.3	+0.2	-3.9	-2.5	-1.3

proposed approach is able to converge towards unique and consistent solutions accordingly. A summary of the initial design variables and their corresponding optimized solutions for the different initial configurations are presented in Table 4 for reference.

Experimental Validation

Once internal defects inside a component are detected using the proposed image-based tomography method, the updated model, which includes the detected defects, should be able to describe the future behavior of the component under future loads. To evaluate the updated model under new loads, the numerical model of the coupon was used to predict strain measurements for comparison with DIC results (Fig. 12). The new loading included a displacement-controlled tensile load applied using the testing machine as a separate test from those used in the updating process. Again, configuration 2 was used as the defective test specimen for this validation. Table 5 shows the comparison of strains at six selected regions of the specimen with those predicted using both the initial and updated models at the load level of 40% of the yielding load. This table shows a very good agreement (<10% maximum

difference) between strains from the updated model and the experimental results. As expected, the error between the experimental and numerical values decreases significantly when using the updated model compared with the initial model. This verifies the effectiveness of the proposed approach in extracting the true properties of a component, which can be used for more realistic prediction of its response under future loads.

Limitations and Future Works

The results presented in this paper demonstrated the feasibility of the proposed technique to identify regions with unseen embedded defects via sensing the disturbances in the surface response of a component and updating a FEM model to reflect its internal and external conditions. However, a number of factors regarding the range of applicability and practical aspects of its implementation should be further studied in the future. For example, the effect of internal damage on the external response perturbations is expected to decrease with a reduction in the size and severity of the damage and with an increase in its distance from the surface. In other words, this



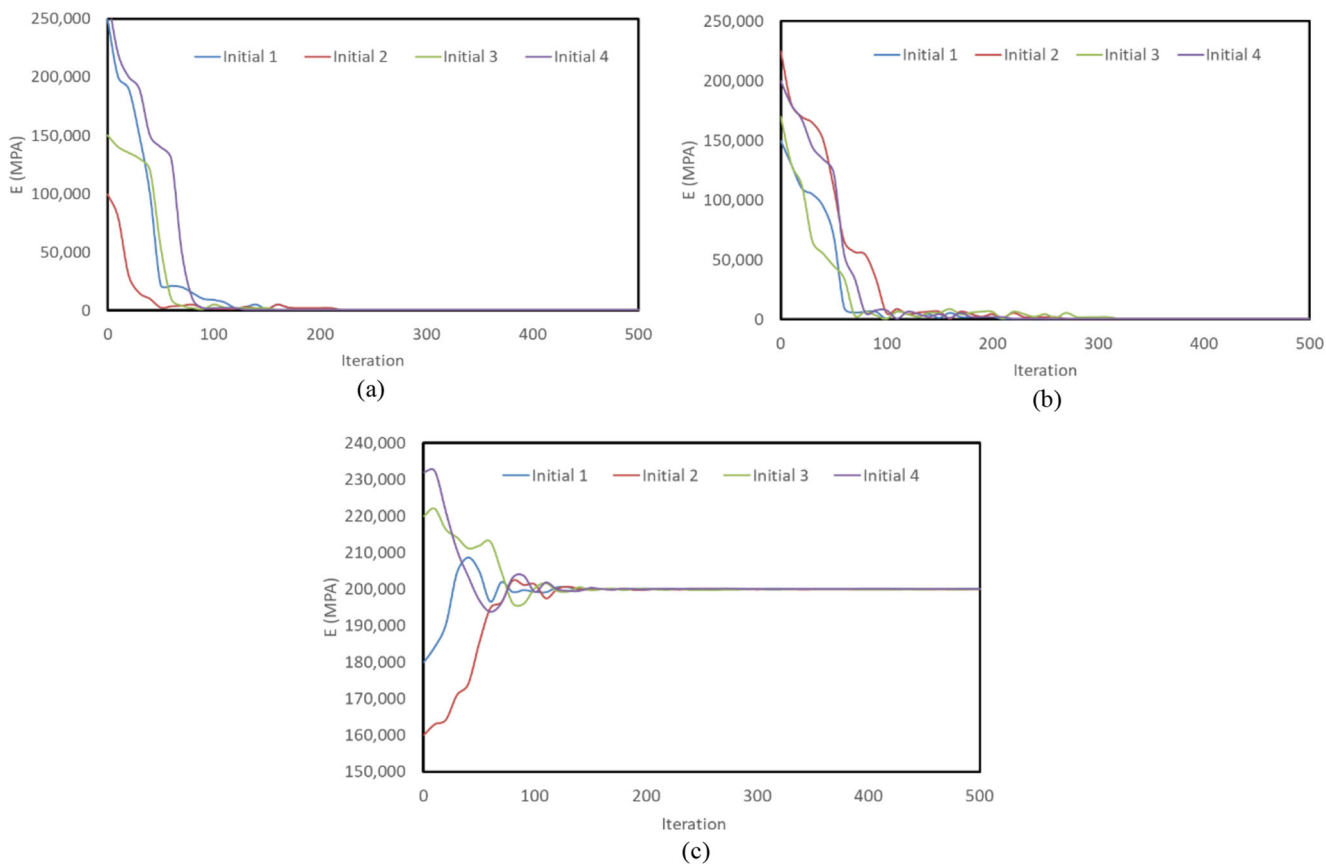


Fig. 10 Initializing the optimization procedure with different start point (a) the convergence of E_1^{ADS} , (b) the convergence of E_2^{ADS} , and (c) the convergence of E_3^{IS}

technique is expected to be able to detect defects above a certain severity and distance threshold, the limits of which should be studied in the future. It should be noted however, that this is similar to most nondestructive evaluation techniques and knowledge about the range of applicability will guide its future applications.

This paper showed the capability to detect the existence and locate the vicinity of voids by dissecting the specimen into a number of partitions whose stiffness is identified within the optimization process. The extension of the proposed method to include the stiffness of each individual finite element as

an unknown design variable can lead to much-finer resolution of detections. In other words, a topology optimization extension should update the stiffness of each individual element, thus producing a “stiffness map” throughout the entire volume of the specimen. The resulting stiffness map should then in theory be able to point to a variety of defects such as voids (regions with negligible stiffness), inclusions (anomalies in stiffness), delamination and cracks (planar or layer-wise discontinuity in stiffness). In practice, however, future experimental work with different defect types needs to be carried out to demonstrate the range of applicability of the method

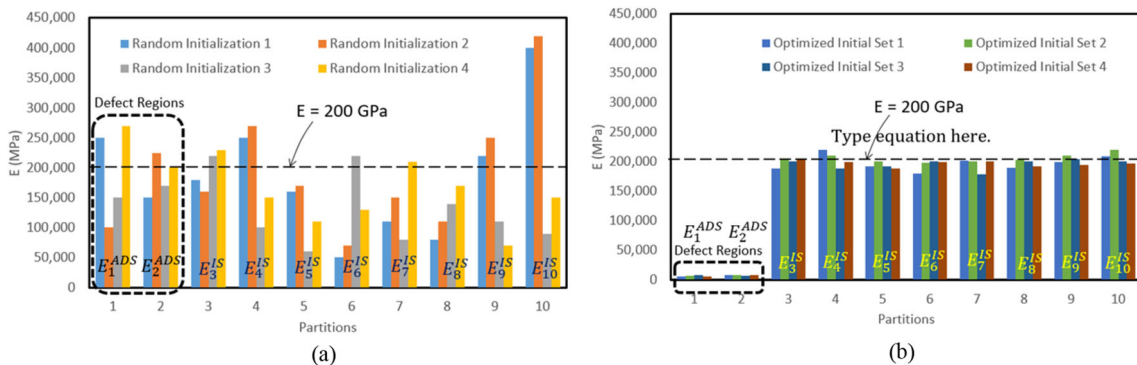


Fig. 11 Comparison of initial and final properties for partitions within CF2 (a) initial properties, (b) final properties

Table 5 Longitudinal strain comparison of the experimental results with initial and updated model predictions at 40% of yield stress (CF 2)

Selected Regions	Initial Model ($\mu\epsilon$)	DIC-Initial / DIC (%)	Updated Model ($\mu\epsilon$)	DIC-Updated / DIC (%)	DIC results ($\mu\epsilon$)
1	655	41.9	987	12.5	1128
2	744	66.0	412	8.0	448
3	698	25.0	887	5.4	938
4	877	15.0	702	7.8	762
5	698	60.0	392	10.0	436
6	790	33.0	1102	7.0	1185

with respect to defect types. This also applies to the assumption and choice of material models and constitutive properties considered in the optimization. While this paper used a simple homogenous steel coupon within its linear elastic region, other parametrizations and more complicated materials can also be investigated in the future, while taking into account the associated numerical convergence implications.

In terms of practical implications, as this technique relies on surface measurements using DIC, the surface of the specimen needs to undergo surface preparation (e.g., random high-contrast speckle pattern). This may in turn affect the applicability of the technique for large-scale structural components which may require sizable surface preparation and multiple sets of camera systems. While laboratory-scale feasibility was shown in this paper, successful use of DIC for large-scale structures such as wind turbines in the literature [44] is evidence for the potential of the technique at larger scales. Finally, it was stated that the main advantage of the proposed technique over internal 3D scanning (e.g., XCT) is its reliance on regular cameras and the reduced need for specialized sensing equipment and expertise. However, this comes at the expense of increased computational demand for FEM modeling, optimization, and DIC postprocessing.

In order to investigate and extend the range of applicability of the proposed method beyond the small-scale, uniaxial configuration of the homogenous steel specimen tested herein,

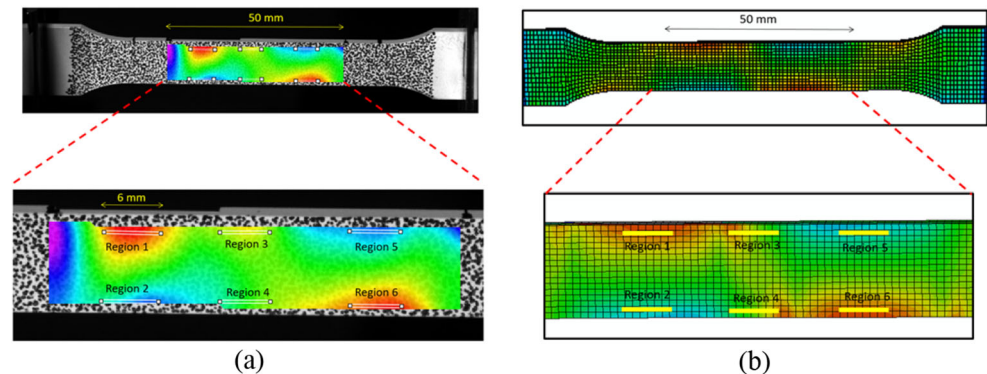
future work is required to study its performance across a variety of structural configurations such as large-scale, complex, and multi-member structures, composed of different materials such as reinforced concrete and composites. Study of such complex examples will shed light on the identification capabilities of the proposed technique in the presence of confounding unknowns such as internal non-homogeneities, delamination and rebar corrosion. Further comparison with internal 3D scanning techniques in terms of identification range and accuracy, practical issues, and costs can also highlight the potential benefits of the proposed technique for future applications.

Conclusion

The purpose of this preliminary investigation was to evaluate the feasibility of leveraging full-field measurements for structural identification, with the goal of recovering the volumetric interior defect distribution in structural components. Within this image-based tomography framework, steel coupon specimens with simulated defects were used to evaluate the performance of the structural identification approach that utilized an inverse approach to identify unknown and uncertain constitutive properties of the material based on full-field deformation measurements correlated with FEM predictions.

Digital Image Correlation was utilized to extract full-field deformation measurements of the test specimen, subjected to

Fig. 12 Prediction correspondence between experimental and undated numerical results (a) 3D DIC results at load level of 40% of yield, (b) FEM modeling results at load level of 40% of yield



standard ASTM E8 tensile testing, with the measurements collected of only the intact surface (i.e. simulated defect unseen by the cameras). The corresponding FEM models of the specimens were divided into a set of regions with uniform modulus of elasticity, each of which had random initial stiffness values. To establish the FEM model updating scheme, the ABAQUS solver was interfaced with an optimization package and the unknown parameters were adjusted iteratively until finding the optimal values. The optimization strategy leverages a genetic algorithm to perform the global search and a limited-memory Broyden-Fletcher-Goldfarb-Shanno scheme for the local search for the optimal solution parameters. As a result of the optimization process, all of the intact regions converged to elastic modulus close to the expected value of 200 GPA for A36 steel, with the exception of the defect regions that showed a dramatic reduction in elastic modulus, which approached the expected value of zero for a void. These outcomes demonstrated the ability of the proposed image-based tomography framework to identify internal defects in the form of anomalies in material constitutive properties. Moreover, to evaluate the uniqueness of the solution in the proposed approach, different sets of initial values were selected to show the insensitivity of the results to the selected initial values. The results showed that, even though the initial points were selected randomly for the 4 different sets, the proposed algorithm had the capability to converge to the optimal values. The results of this preliminary investigation and the ability of the proposed method to detect internal abnormalities hint at the possibility of determining not only the material distribution of a specimen, but also determining the location, dimensions, and shape of the defect. The results of this paper are encouraging and may open up new opportunities to characterize heterogeneous materials for their mechanical property distribution.

Declarations

Conflict of Interest On behalf of all authors, the corresponding author states that there is no conflict of interest.

References

- Alfirević I (1995) Strength of materials. I. Tehnička knjiga. ISBN 953-172-010-X
- Drucker DC (1967) Introduction to mechanics of deformable solids. McGraw-Hill
- Timoshenko S (1976) Strength of materials, 3rd edition. Krieger Publishing Company, ISBN 0-88275-420-3
- ASTM International (2016) Standard test methods for tension testing of metallic materials, ASTM E8 / E8M-16a. West Conshohocken, Pennsylvania
- Li H, Weiss W, Medved M, Abe H, Newstead GM, Karczmar GS, Giger ML (2016) Breast density estimation from high spectral and spatial resolution. *MRI J Med Imaging* 3, 044507
- Mei Y, Goenezen S (2015) Spatially weighted objective function to solve the inverse problem in elasticity for the elastic property distribution. In: Doyle B, Miller K, Wittek A, Nielsen PMF (eds) *Computational biomechanics for medicine: new approaches and new applications*. Springer, New York
- Mei, Y.; Goenezen, S. Parameter identification via a modified constrained minimization procedure. In *Proceedings of the 24th International Congress of Theoretical and Applied Mechanics*, Montreal, QC, Canada, 21–26 August 2016
- Mei Y, Kuznetsov S, Goenezen S. Reduced boundary sensitivity and improved contrast of the regularized inverse problem solution in elasticity. *J Appl Mech* 2015, 83
- Bayat M, Denis M, Gregory A, Mehrmohammadi M, Kumar V, Meixner D, Fazzio RT, Fatemi M, Alizad A (2017) Diagnostic features of quantitative comb-push shear elastography for breast lesion differentiation. *PLoS One* 12:e0172801
- Bayat M, Ghosh S, Alizad A, Aquino W, Fatemi M (2016) A generalized reconstruction framework for transient elastography. *J Acoust Soc Am* 139:2028
- Wang M, Dutta D, Kim K, Brigham JC (2015) A computationally efficient approach for inverse material characterization combining Gappy POD with direct inversion. *Comput Methods Appl Mech Eng* 286:373–393
- Bay BK, Smith TS, Fyhrie DP, Saad M (1999) Digital volume correlation: three-dimensional strain mapping using X-ray tomography. *Exp Mech* 39(3):217–226
- Smith TS, Bay BK, Rashid MM (2002) Digital volume correlation including rotational degrees of freedom during minimization. *Exp Mech* 42(3):272–278
- Gates M, Lambros J, Heath MT (2011) Towards high performance digital volume correlation. *Exp Mech* 51(4):491–507
- Franck C, Hong S, Maskarinec SA, Tirrell DA, Ravichandran G (2007) Three-dimensional full-field measurements of large deformations in soft materials using confocal microscopy and digital volume correlation. *Exp Mech* 47(3):427–438
- Germaneau A, Doumalin P, Dupre J-C (2007) 3D strain field measurement by correlation of volume images using scattered light: recording of images and choice of marks. *Strain* 43(3):207–218
- Roux S, Hild F, Viot P, Bernard D (2008) Three-dimensional image correlation from x-ray computed tomography of solid foam. *Compos Part A-Appl S* 39(8):1253–1265
- Yang Z et al (2017) In-situ X-ray computed tomography characterisation of 3D fracture evolution and image-based numerical homogenisation of concrete. *Cem Concr Compos* 75:74–83
- Mei Y, Goenezen S. "Non-Destructive characterization of heterogeneous solids from limited surface measurements." 24th International Congress of Theoretical and Applied Mechanics, Montreal, QC, Canada, Aug. 2016
- Mei Y et al (2016) Estimating the non-homogeneous elastic modulus distribution from surface deformations. *Int J Solids Struct* 83: 73–80
- Mei Y, et al. "Mechanics based tomography: a preliminary feasibility study." *Sensors* 17.5 (2017): 1075
- Luo P et al (2018) Characterization of the stiffness distribution in two- and three-dimensions using boundary deformations: a preliminary study. *MRS Communications* 8(3):893–902
- Peddle J, Goudreau A, Carson E et al (2011) Bridge displacement measurement through digital image correlation. *Bridge Struct* 7(4): 165–173
- Citto C, Shan IW, Willam K, Schuller MP (2011) In-place evaluation of masonry shear behavior using digital image analysis. *ACI Mater J*, 108(4)

25. Murray CA, Hoag A, Hoult NA (2015) Take WA (2014) field monitoring of a bridge using digital image correlation. *Proceedings of the ICE - Bridge Engineering* 168(1):3–12
26. Vaghefi K, Ahlborn TM, Harris DK, Brooks CN (2015) Combined imaging Technologies for Concrete Bridge Deck Condition Assessment. *J Perform Constr Facil* 29(4):04014102
27. Chemisky Y, Meraghni F, Bourgeois N, Cornell S, Echchorfi R, Patoor E (2015) Analysis of the deformation paths and thermomechanical parameter identification of a shape memory alloy using digital image correlation over heterogeneous tests. *Int J Mech Sci* 96:13–24
28. Coppieters S, Hakoyama T, Debruyne D, Takahashi S, Kuwabara T (2018). Inverse yield locus identification of sheet metal using a complex cruciform in biaxial tension and digital image correlation. In *Multidisciplinary digital publishing institute proceedings* (Vol. 2, no. 8, p. 382)
29. Blaber J, Adair B, Antoniou A (2015) Ncorr: open-source 2D digital image correlation MATLAB software. *Exp Mech* 55(6):1105–1122
30. Lionello G, Cristofolini L (2014) A practical approach to optimizing the preparation of speckle patterns for digital-image correlation. *Meas Sci Technol* 25(10):107001
31. Dizaji MS, Alipour M, Harris D (2018) Leveraging full-field measurement from 3D digital image correlation for structural identification. *Exp Mech*:1–18
32. Dizaji MS, Harris D, Alipour M, Ozbulut O. En “vision” ing a novel approach for structural health monitoring—a model for full-field structural identification using 3D–digital image correlation. *The 8th international conference on structural health monitoring of intelligent infrastructure, Bridbane, Australia2017*. p. 5–8
33. Dizaji MS, Alipour M, Harris DK (2017) Leveraging vision for structural identification: a digital image correlation based approach. Springer, *International Digital Imaging Correlation Society*, pp 121–124
34. Dizaji MS, Harris DK, Alipour M, Ozbulut OE. Reframing measurement for structural health monitoring: a full-field strategy for structural identification. *Nondestructive Characterization and Monitoring of Advanced Materials, Aerospace, Civil Infrastructure, and Transportation XII: International Society for Optics and Photonics*; 2018. p. 1059910
35. Correlated Solutions Inc (2005) VIC-3D user manual. Correlated Solutions, Columbia
36. Abaqus Inc (2018) ABAQUS theory manual, version 6.6. Simulia, Providence
37. An introduction to script writing in ABAQUS software, <http://bertoldi.seas.harvard.edu/files/bertoldi/files/learnabaquusscriptinonehour.pdf>
38. Goldberg DE (1989) *Genetic algorithm in search, optimization and machine learning*. Addison-Wesley, Reading
39. Jung DS, Kim CY (2013) Finite element model updating of a simply supported skewed PSC I-girder bridge using hybrid genetic algorithm. *KSCE J Civ Eng* 17(3):518–529
40. Joghataie A, Farrokh M (2008) Dynamic analysis of non-linear frames by Prandtl neural networks. *J Eng Mech* 134(11):961–969
41. Farrokh M, Shafiei Dizaji M, Joghataie A (2015) Modeling hysteretic deteriorating behavior using generalized Prandtl neural network. *J Eng Mech* 141(8):040150
42. Ghouati O, Gelin JC (1997) An inverse approach for the identification of complex material behaviours. In: Sol H, Oomens CWJ (eds) *Material identification using mixed numerical experimental methods*. Kluwer Academic Publishers, Dordrecht, pp 93–102
43. Meuwissen M, Oomens C, Baaijens F, Petterson R, Janssen J (1997) Determination of parameters in elasto-plastic models of aluminium. In: Sol H, Oomens CWJ (eds) *Material identification using mixed numerical experimental methods*. Kluwer Academic Publishers, Dordrecht, pp 71–80
44. LeBlanc B, Niezrecki C, Avitabile P, Chen J, Sherwood J (2013) Damage detection and full surface characterization of a wind turbine blade using three-dimensional digital image correlation. *Struct Health Monit* 12(5–6):430–439

Publisher's Note Springer Nature remains neutral with regard to jurisdictional claims in published maps and institutional affiliations.

